Journal of Materials Chemistry A

# Enhanced Oxygen Evolution Catalyzed by In-Situ Formed Fe-Doped Ni Oxyhydroxides in Carbon Nanotubes

| | |
|---|---|
| Journal: | *Journal of Materials Chemistry A* |
| Manuscript ID | TA-ART-05-2022-004042.R1 |
| Article Type: | Paper |
| Date Submitted by the Author: | 20-Jun-2022 |
| Complete List of Authors: | Chen, Dandan; Wenzhou University, Chemistry and Materials Engineering<br>Sun, Qiuhong; Wenzhou University, Chemistry and Materials Engineering<br>Han, Cheng; Wenzhou University, Chemistry and Materials Engineering<br>Guo, Yuanyuan; Wenzhou University<br>Huang, Qi; Wenzhou University, a. Key Laboratory of Carbon Materials of Zhejiang Province, College of Chemistry and Materials Engineering,<br>Goddard III, William; California Institute of Technology,<br>Qian, Jinjie; Wenzhou University, College of Chemistry and Materials Engineering; Chinese Academy of Sciences Fujian Institute of Research on the Structure of Matter, State Key Laboratory of Structural Chemistry |
| | |

SCHOLARONE™
Manuscripts

# Enhanced Oxygen Evolution Catalyzed by In-Situ Formed Fe-Doped Ni Oxyhydroxides in Carbon Nanotubes

Dandan Chen[a], Qiuhong Sun[a], Cheng Han[a], Yuanyuan Guo[a], Qi Huang[a], William A. Goddard, III*[b] and Jinjie Qian*[a]

[a]Key Laboratory of Carbon Materials of Zhejiang Province, College of Chemistry and Materials Engineering, Wenzhou University, Wenzhou, Zhejiang, 325035, P. R. China

[b]Materials and Process Simulation Center (MSC), MC 139-74, California Institute of Technology, Pasadena, California 91125, United States

*Corresponding author

E-mail: jinjieqian@wzu.edu.cn; wag@caltech.edu

**Abstract**

The rational design and preparation of cost-effective, efficient and durable metal carbon nanomaterials for oxygen evolution reaction (OER) is of great urgency. Herein, we report a high-performance OER electrocatalyst consisted of bimetallic $FeNi_3$ nanoparticles encapsulated in hierarchical carbon nanomaterial, denoted as **$FeNi_3$@NCNT**. Through a stepwise strategy, hollow carbon nanorods with abundant carbon nanotubes can be successfully calcined from rod-like **NiOF-1-Fe**, which are hydrolyzed to these initial **NiOF-1** by Fe(III) ions. The optimal **$FeNi_3$@NCNT** catalyst exhibits an excellent electrochemical performance with a low overpotential of 264 mV at 10 mA $cm^{-2}$, a Tafel slope of 58.5 mV $dec^{-1}$, and a robust stability over 10 hours compared to control samples. This enhanced OER arises from the unique hollow nanorod modified with nanotube structure, large surface area, rich nitrogen content, and the synergistic effect between Ni and Fe species. Indeed, it is catalyzed by *in-situ* generated Fe coupling with NiOOH in carbon nanotubes, which is validated by the subsequent theoretical calculations. This work enables insights into the mechanism of Fe-doped Ni oxyhydroxides for efficient OER and adds to the increasing understanding for design and synthesis of novel catalysts for efficient energy conversion and storage.

**Keywords:** Metal-organic framework; Carbon nanotube; $FeNi_3$ alloy; Fe-doped Ni oxyhydroxide; Oxygen evolution.

## 1. Introduction

The excessive consumption of fossil fuels and the increasingly serious global environmental issues make it most urgent to exploit renewable clean energy. Under these circumstances, green hydrogen energy features no pollution, high specific energy density, and abundant resource which is regarded as the most suitable alternative to conventional fossil fuels.[1] [2] [3] Although water-splitting is an advanced technology for hydrogen production, the sluggish kinetics of the oxygen evolution reaction (OER) at the anode significantly impedes practical industrial applications.[4] Thus, it is paramount role in to decrease the overpotential for OER, and boost the catalytic efficiency.[5] [6] [7] [8] The currently commercial noble metal based oxides are recognized as the state-of-the-art catalysts because of their high activity and selectivity towards OER, but their high cost and scarcity severely limit large-scale utilization.[9] [10] This has led to exploring high-efficiency, cost-effective and robust non-noble metal based OER electrocatalysts to provide the basis for application of water electrolysis toward attaining a cleaner environment.

Metal-organic frameworks (MOFs) are a well known subclass of highly crystalline coordination polymers, which are easily self-assembled by metal nodes combined with organic linkers.[11] Because of their high porosity, well-defined nanostructures, and adjustable topologies, MOF materials have demonstrated great potential as self-supporting or self-sacrificing templates and precursors.[12] [13] For example, through controllable thermal treatment and wet chemical engineering, various nanoarchitectures can be easily achieved.[14] Unfortunately the present, porous carbon-based catalysts obtained from direct pyrolysis of MOF precursors provide limited electrocatalytic properties due to the low utilization rate of

internal active species and the inferior mass/electron transfer efficiency. Compared with these bulk materials, hollow nanosized composites provide much ore favorable characteristics of faster mass transfer, richer active components, higher exposure rate of active sites, and better compatibility.[15] However, it remains a challenging task to design and synthesize hollow MOF-derived nanomaterials possessing unique open structures, which require a suitable etching agent or protective agent that combines suitably with the features of MOFs.[16] [17] For instance, Yamauchi *et al*. reported a novel hollow nanostructured ZIF-67 framework by a moderate anisotropic surface modification and etching procedure using cyanuric acid.[18] Meanwhile, Li and co-workers demonstrated a two-step pyrolysis-oxidation method to prepare cobalt-based nanoparticles (NPs) embedded into hollow N-doped carbon calcined from ZIF-67 for efficient OER.[19] Similarly, our group previously reported that a type of hollow FeNiP/C-900 can be obtained by pyrolysis of three-dimensional hollow barrel-like BMM-10 under strong etching effect by Fe(III), which achieves a high current density with a low overpotential during OER electrolysis.[20]

On the other hand, the *in-situ* thermal conversion of MOF crystals to carbon nanotube (CNT) based composites has proved to be an effective strategy to promote electrocatalytic performance.[21] [22] [23] Over the past few years, Liu and his collaborators have designed a distinctive Co/$Co_2P$ NPs encapsulated in N,P-doped CNTs (Co/$Co_2P$@NPCNTs) by the mechanochemistry-pyrolysis method, which shows competitive performance to the commercial Pt/C and $RuO_2$.[24] Meanwhile, Qian *et al*. reported an approach for vegetating ZIF-67 polyhedra onto an indium-based InOF-1 to fabricate carbon nanorods coated with rich N-doped CNTs after calcination, which reveals excellent OER performance with only 270 mV

overpotential at 10 mA $cm^{-2}$.[25] More significantly, there are several strategies for efficient growth of CNTs from MOF materials, such as growing CNTs by *in-situ* conversion of MOFs, catalyzing CNTs by exogenetic metal catalysts and/or carbon sources, developing CNTs on MOF-coated substance, and applying multiple calcination treatments.[26] [27] Although some progresses has been made, great opportunities and challenges remain in the synthesis of nanocomposites to combine hollow nanostructures and highly graphitized CNTs.

In the work reported here, we obtained a unique type of hierarchical hollow carbon nanomaterial modified with dense multi-walled CNTs derived from nickel-organic framework (**NiOF-1**) nanorods, denoted as **$FeNi_3$@NCNT**. To achieve this we developed an innovative controllable solvothermal method that combines an etching function with a calcination process (**Scheme 1**). Significantly, the as-synthesized **$FeNi_3$@NCNT** exhibits an superior OER performance with an overpotential of 264 mV at 10 mA $cm^{-2}$ and a Tafel slope of 58.5 mV $dec^{-1}$ in 1.0 M KOH. In comparison with control samples, the enhanced electrocatalytic performance arises the cooperative effect of bimetallic alloys that are evenly

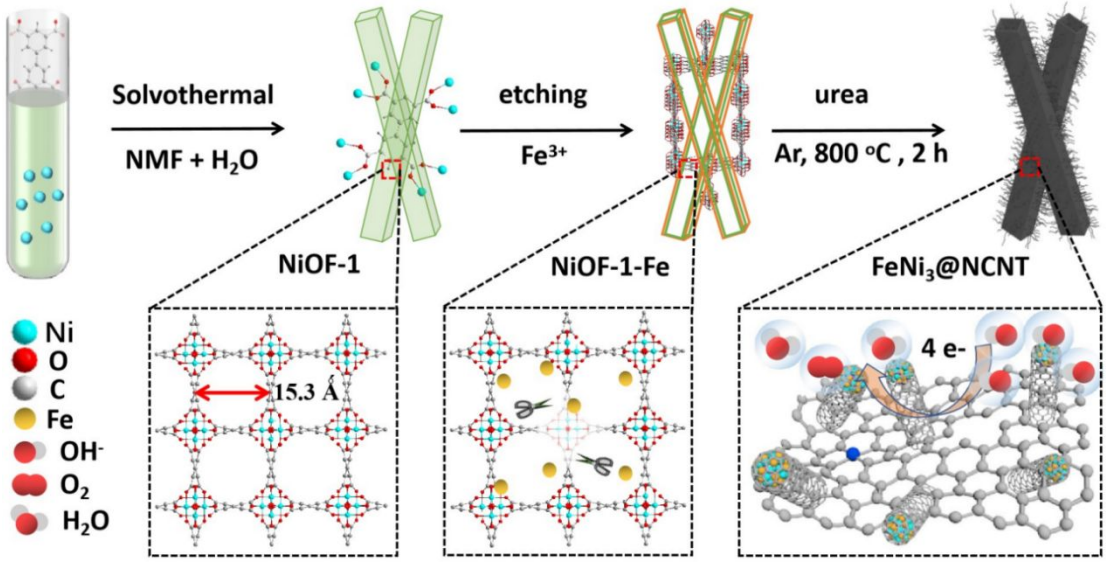


**Scheme 1** The synthetic route to obtain the efficient **$FeNi_3$@NCNT** OER catalyst.

dispersed in the porous hollow MOF-derived carbon composite. This results in minimal current attenuation over the 10 hours continuous durability test. Furthermore, we applied density functional theory (DFT) calculations to construct the relevant theoretical models to confirm this dramatic improvement of OER. This study provides a new approach for exploration of high-activity and durable OER catalysts, needed for developing clean energy.

## 2. Results and Discussion

In the single-crystal structure, each fully deprotonated $BPTC^{4-}$ connects to eight independent Ni(II) atoms, which has a 6-coordinate octahedron geometry composed of four carboxylate oxygen atoms together with two $\mu_2$-$H_2O$ molecules (**Figure 1a, S1**). These tetracarboxylates are further partnered with 1-dimensional Ni-O chains to constitute tetragonal cylindrical channels of approximately 15.3 Å along the *c* axis. This structure shows a large aspect ratio

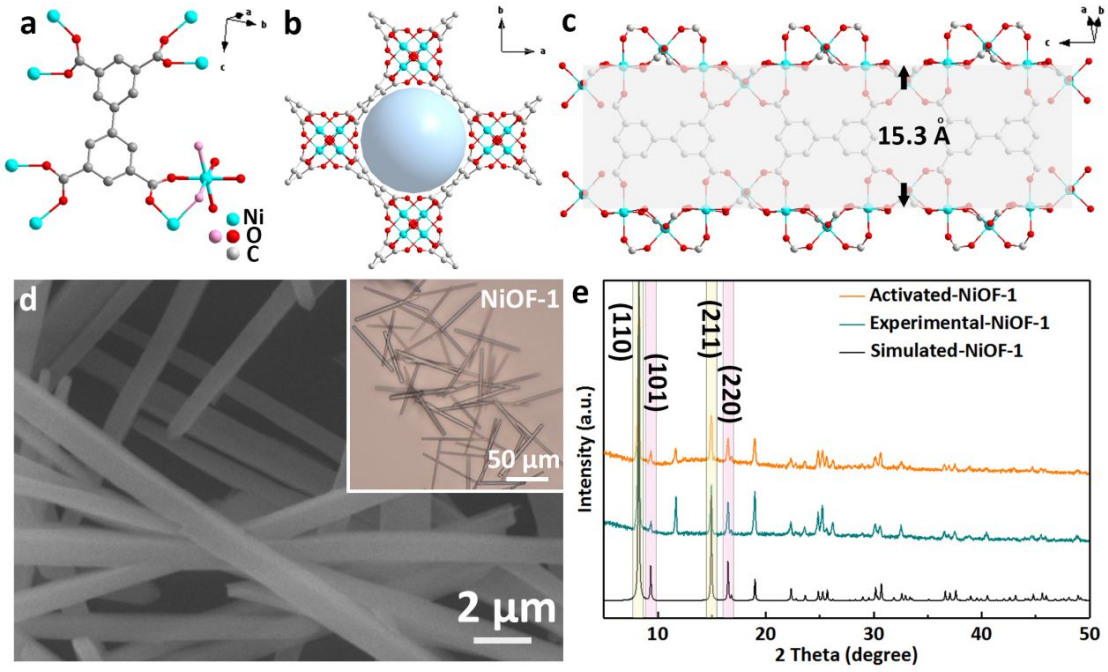


**Figure 1** (a) Coordination environment of the $BPTC^{4-}$ linker and Ni(II) center in **NiOF-1**. (b) The 3-dimensional tetragonal channel. (c) The cylindrical channel along the *c* axis. (d) SEM/optical images, and (e) PXRD patterns of **NiOF-1**.

with the rod-like morphology, which enables this microporous MOF precursor to form a nanosized template (**Figure 1b-1c, Table S1**).[28] [29] In **Figure 1d, S2**, these as-obtained **NiOF-1** nanorods exhibit a highly crystalline structure with smooth surfaces, as confirmed with scanning electron microscopy (SEM) and optical photography. Furthermore, the powder X-ray diffraction (PXRD) patterns of experimental and desolvated samples are consistent with the simulations, but the diffraction peak intensity of the activated sample is relatively weaker, which is ascribed to partial decomposition after desolvation. In this case, the diffraction peaks at 8.2°, 9.3° 14.9° and 16.5° are well indexed to the (110), (101), (211) and (220) crystal planes, respectively (**Figure 1e**).

Based on the special inorganic M-O chain, large aspect ratio morphology, and high chemical stability, these **NiOF-1** nanorods provide an excellent template to generate intriguing nanostructures, as in the following treatment. **Figure 2a** illustrates the successful transformation of a solid structure into its tube-like counterpart. Both the shell and the core of Ni-MOF are fabricated by versatile coordination bonds between metal nodes (M) and organic ligands (L). In the outer shell, the relatively stable hydration of -L-M-L-M-$OH_2$ is preferentially formed to protect against further damage of M-L bonds. By contrast, the metastable structure of -M-L-M-L results in a partial decomposition due to hydrolysis of Fe(III). Therefore, the overall construction continually collapses with production of $M(OH)_n$ species in which the shell is retained, while the core is dissolved to obtain the hollow **NiOF-1-Fe**. SEM and transmission electron microscopy (TEM) images show the preserved tubular shape with a mildly dilapidated surface but a relatively complete framework, **Figure 2b, S3**. We selected randomly a single nanorod for line scanning and found less Ni and Fe contents in the core

layers compared with the shell (**Figure 2c**). In **Figure 2d**, the PXRD pattern of the etched sample retains characteristic peaks, but the diffraction intensity is reduced as the crystallinity is partially destroyed. Fourier transform infrared (FT-IR) analysis was performed, finding that peak intensities of =C-H bending vibrations at 1050-1150 $cm^{-1}$ and C-H stretching vibrations at 2500-2700 $cm^{-1}$ are much weaker than for the pure $H_4$BPTC (**Figure 2e**). Here, the signal at 3285 $cm^{-1}$ is assigned to the O-H stretching vibration, demonstrating protection of the shell layer with hydration of $H_2O$. In the Raman spectra of **Figure 2f**, the two strong bands at 1605 and 1004 $cm^{-1}$ are reasonably attributed to aromatic-ring stretching vibrations and in-plane symmetric C-H bending vibration of the

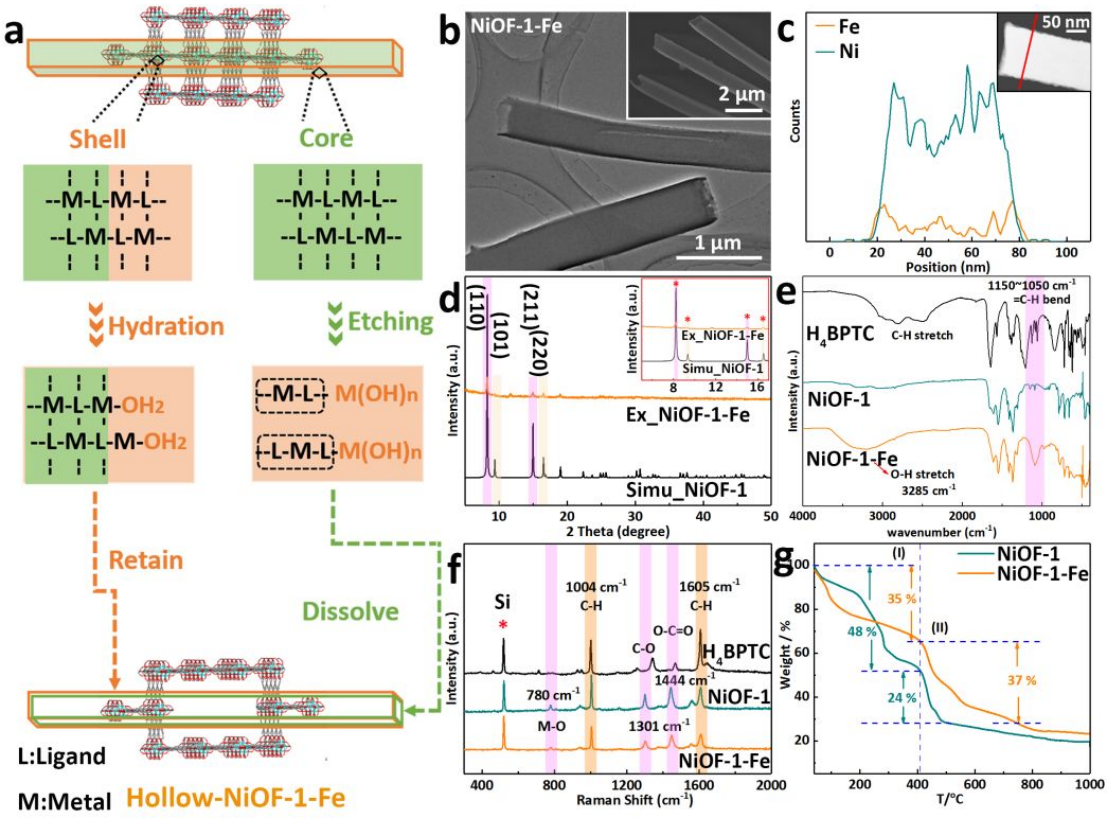


**Figure 2** (a) The etching mechanism to form hollow **NiOF-1-Fe**. (b) TEM/SEM images of **NiOF-1-Fe**. (c) Line profile of one etched nanorod. (d) PXRD patterns. (e/f) FT-IR/Raman spectra. (g) TGA curves of **NiOF-1** and **NiOF-1-Fe**.

organic linker. The O-C=O vibration peak at 1444 $cm^{-1}$ arises from deprotonation of the carboxylic groups, and one new peak at 780 $cm^{-1}$ involves metal-oxygen bond vibration.[30] In **Figure 2g**, both **NiOF-1** and **NiOF-1-Fe** reveal that two major weight loss feature in the thermogravimetric analysis (TGA): the first loss corresponds to volatilization of solvents with sequential decomposition of $BPTC^{4-}$. The second loss after 410 $^{o}C$ is ascribed to the complete carbonization of organic precursors to porous carbon. Furthermore, both the desolvated **NiOF-1** and the etched **NiOF-1-Fe** exhibit Type-IV isotherms indicative of abundant pores, which was confirmed by the pore size distribution (PSD, **Figure S4**).

These hollow **NiOF-1-Fe** precursors are pyrolyzed with the addition of urea as the nitrogen source to obtain $FeNi_3$ NPs inside the N-doped CNTs, denoted as **$FeNi_3$@NCNT**. First, its hollow tubular shape remains where a large number of dense multi-walled CNTs are grown onto the surface in **Figure 3a-3b, S8**. The height profile of one single particle verifies the hollow morphology, while the corresponding compositional line profile shows more Ni, Fe and C elements contained in the shell layer (**Figure 3c, 3d**). TEM images of **Figure 3e-3f** distinctly display that the hollow carbon material obtained features a bunch of CNTs stretched out from the tube-like carbon matrix. Interestingly, the metal particles are mainly distributed and encapsulated at the tips of CNTs so that they are conveniently catalyzed by Fe and Ni. Moreover, the high-resolution TEM (HR-TEM) image gives the characteristic spacings of 0.21 and 0.35 nm for the (111) and (100) facets for $FeNi_3$, respectively, and 0.34 nm for the (002) plane of graphitic carbon (**Figure 3g**). On the other hand, energy-dispersive X-ray spectroscopy (EDX) in **Figure 3h** certifies the co-existence of Ni, Fe, C, N, and O elements (**Table S3**). Further the high-angle annular dark-field scanning TEM

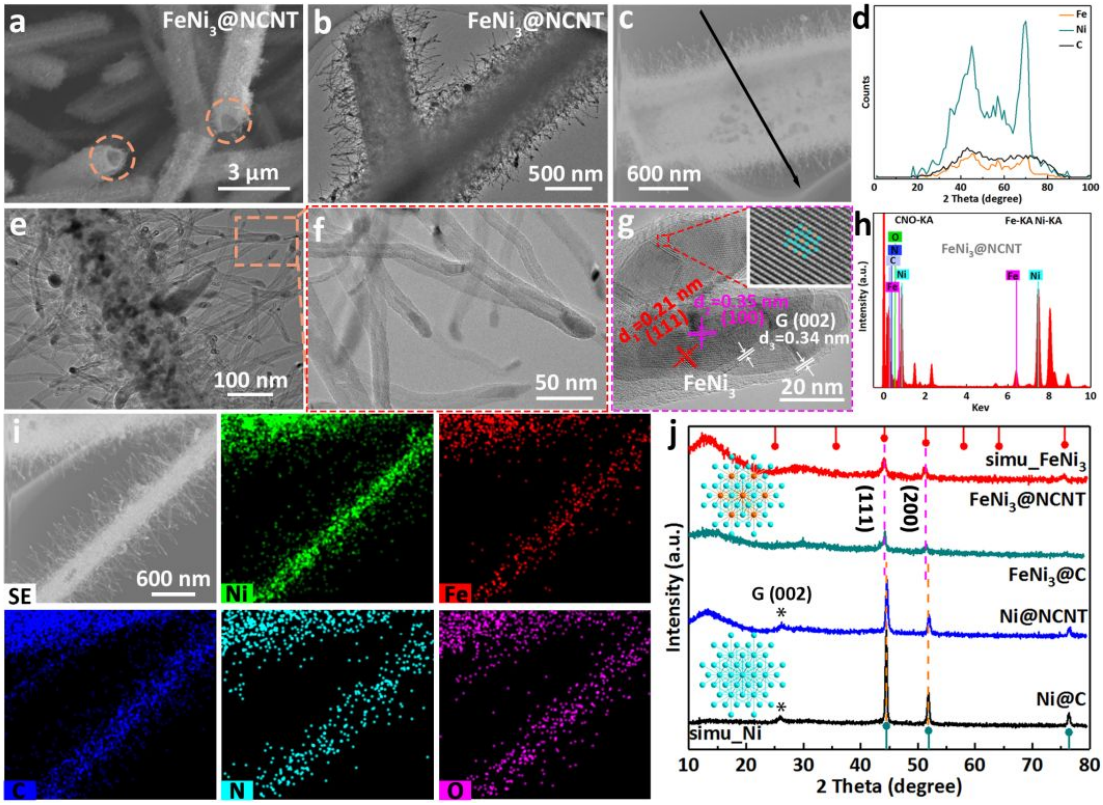


**Figure 3** (a, b, e-g) SEM, TEM and HR-TEM images of **$FeNi_3$@NCNT**. (c-d) The height profile, (h) The EDX pattern, (i) The HAADF-STEM, and element mapping images of **$FeNi_3$@NCNT**. (j) PXRD patterns of MOF-derived carbon nanomaterials.

(HAADF-STEM) and its corresponding element mapping images, clearly confirm the even distribution of these five elements in **$FeNi_3$@NCNT** (**Figure 3i**). Finally, all the diffraction patterns exhibit three main peaks at 44.12°/44.50°, 51.40°/51.84°, and 75.66°/76.37° indexed to the (111), (200), and (220) lattice planes of $FeNi_3$/Ni (PDF#65-3244/04-0850), respectively, in accord with the HR-TEM analyses (**Figure 3j**). For the detailed features of other control samples, including **Ni@C**, **Ni@NCNT**, **$FeNi_3$@C**, please refer to **Figure S5-S11**.

X-ray photoelectron spectroscopy (XPS) characterization was carried out to further analyze the chemical state on the surface. In **Figure 4a**, the full survey XPS spectra validate the co-existence of Ni, C, N and O in all these as-pyrolyzed carbon nanocomposites, except Fe only

for **$FeNi_3$@C** and **$FeNi_3$@NCNT**. In this case, the high-resolution Ni 2p spectra clearly show the presence of metallic Ni(0) at 851.8 and 869.9 eV and a predominant doublet at 854.2 and 872.2 eV of Ni(II) $2p_{3/2}$ and $2p_{1/2}$, respectively. Furthermore, negatively shifted binding energy of 0.6 eV in the $FeNi_3$ phase and the pair of shake-up satellite peaks at 861.2 and 879.9 eV can be observed in **Figure 4b**. The deconvoluted Fe 2p curves exhibit two contributions of $2p_{1/2}$ and $2p_{3/2}$, which are located at 706.8/710.5/712.6 and 718.2/724.1/728.4 eV and assigned to the three chemical environments of Fe(0/II/III) in **$FeNi_3$@C** and **$FeNi_3$@NCNT**, respectively (**Figure 4c**).[31] In addition, the broad peak in the C 1s spectra

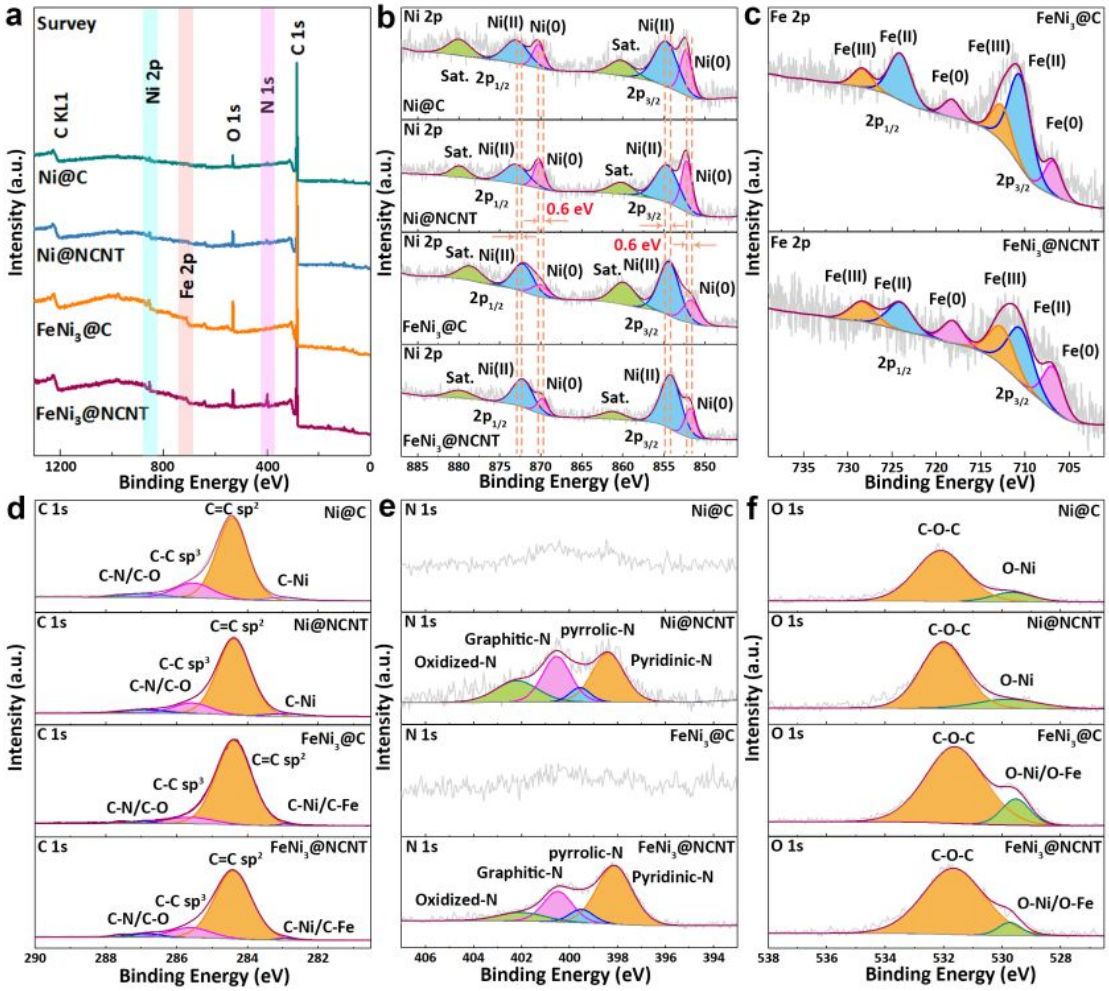


**Figure 4** (a) Full survey XPS spectra, the corresponding deconvoluted XPS spectra of (b) Ni 2p, (c) Fe 2p, (d) C 1s, (e) N 1s, and (f) O 1s.

can be fitted into four peaks at 282.9, 284.4, 285.6, and 286.9 eV in **Figure 4d** that we ascribe to C-Ni/C-Fe, C=C $sp^2$, C-C $sp^3$, and C-N/C-O bonds, respectively. Moreover, we index the four moderate peaks at 398.4, 399.6, 400.7 and 402.2 eV of **$FeNi_3$@NCNT** to pyridinic N, pyrrolic N, graphitic N, and oxidized N, respectively. These higher contents of graphitic/pyridinic N availabilily may facilitate the OER response (**Figure 4e**). Last but not least, we discovered two broad peaks of O-Ni/O-Fe and C-O-C at 529.6 and 531.8 eV, as shown in **Figure 4f**. These results are validated by the XPS results of **Ni@C**, **Ni@NCNT** and **$FeNi_3$@C** that show similar chemical states and surface components compared with **$FeNi_3$@NCNT**, the only differences resulting from the N content and the presence or absence of Fe.

In order to analyze the specific surface areas and pore properties, we conducted $N_2$ adsorption-desorption measurements. All carbon nanomaterials were examined to reveal similar Type-IV characteristics with the particular hysteresis loop in **Figure 5a**, which demonstrates that this series of carbon composites are primarily associated with mesopores and macropores. Moreover the corresponding PSD curves in **Figure 5b** were further calculated by the BJH mode. Furthermore, the Brunauer-Emmett-Teller (BET) surface area and total pore volume ($V_T$) supports the structural features of these porous materials. Comparing with **Ni@C** ($S_{BET}$ = 47.61 $m^2\ g^{-1}$; $V_T$ = 0.2267 $cm^3\ g^{-1}$), **Ni@NCNT** (67.76 $m^2\ g^{-1}$; 0.2398 $cm^3\ g^{-1}$), and **$FeNi_3$@C** (85.28 $m^2\ g^{-1}$; 0.2109 $cm^3\ g^{-1}$), the optimal **$FeNi_3$@NCNT** (101.37 $m^2\ g^{-1}$; 0.3775 $cm^3\ g^{-1}$) possesses the largest surface area and pore volume (**Table S2**). **Figure 5c** displays the Raman spectra with two main peaks at ~1350 and ~1580 $cm^{-1}$, which we assign to the D peak caused by defect and disorder in carbon matrix as well as the G band

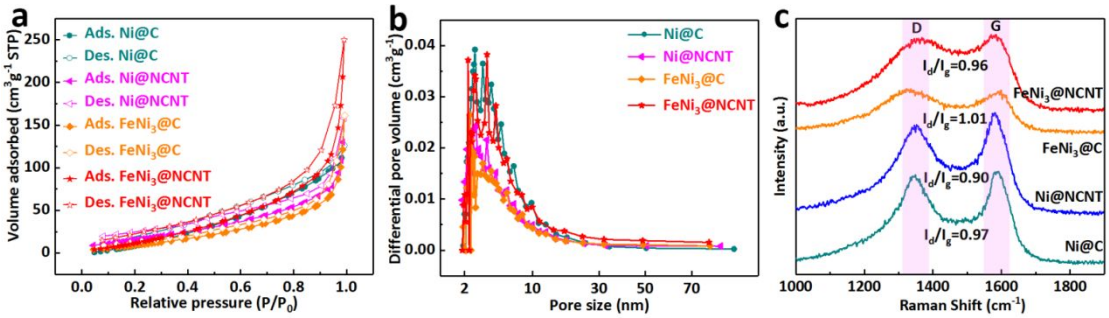


**Figure 5.** (a) $N_2$ sorption isotherms, (b) The corresponding PSD curves, and (c) Raman spectra for **Ni@C**, **Ni@NCNT**, **FeNi$_3$@C** and **FeNi$_3$@NCNT**.

of ordered graphitic carbon network, respectively. In this case, the calculated $I_D/I_G$ value of 0.96 for **FeNi$_3$@NCNT** is larger than for **Ni@CNT** (0.90) but smaller than **FeNi$_3$@C** (1.01). This indicates that the introduction of Fe facilitates an increase in the defects of the carbon layers, while the *in-situ* growth of CNTs promotes the degree of graphitization. Based on the above discussions, we conclude that these catalysts are structurally featured with large active specific surface area, ample pore volume, and high graphitization degree all effectively contributing to enhancing the mass transfer and electrical conductivity in the subsequent electrochemical reactions.

The OER performance was investigated using a three-electrode system, in which the polarization curves are not iR-corrected and the applied potentials have been calibrated into the reversible hydrogen electrode (RHE). The linear sweep voltammetry (LSV), **FeNi$_3$@NCNT** exhibits the lowest overpotential $\eta_{10}$ = 264 mV for 10 mA cm$^{-2}$, much lower than **Ni@C** ($\eta_{10}$ = 360 mV), **Ni@NCNT** ($\eta_{10}$ = 351 mV), **FeNi$_3$@C** ($\eta_{10}$ = 272 mV) and commercial $RuO_2$ ($\eta_{10}$ = 301 mV) (**Figure 6a**). In the continuous LSV tests, the electrochemical performance shows a gradual trend of improvement, which can be attributed to activation of material in the $OH^-$-rich electrolyte, thus forming OER active species of metal oxyhydroxides from inert $FeNi_3$

alloys (**Figure S12**).[32] To verify this hypothesis, we adopted an emulative metal-coordination anion of $SCN^-$ to poison the FeNi-based active sites, leading to the collected inferior LSV curve displayed in **Figure S13**. Moreover, the fitted Tafel slope value of **$FeNi_3$@NCNT** is 58.5 mV $dec^{-1}$ in **Figure 6b**, indicating higher reaction kinetics than that of **Ni@C** (94.6 mV $dec^{-1}$), **Ni@NCNT** (87.1 mV $dec^{-1}$), **$FeNi_3$@C** (83.6 mV $dec^{-1}$) and $RuO_2$ (76.2 mV $dec^{-1}$). Afterwards, these double-layer capacitance ($C_{dl}$) values from the non-Faraday region by cyclic voltammograms were calculated to be 3.68, 3.81, 5.19, 10.11 and 2.45 mF $cm^{-2}$ for **Ni@C**, **Ni@NCNT**, **$FeNi_3$@C**, **$FeNi_3$@NCNT** and $RuO_2$, respectively (**Figure 6c**, **S14**). This implies superior catalytic activity for **$FeNi_3$@NCNT** with the maximum active area matching the above measured specific surface areas. In **Figure 6d**, the electrochemical impedance spectroscopy (EIS) analysis shows that **$FeNi_3$@NCNT** has a

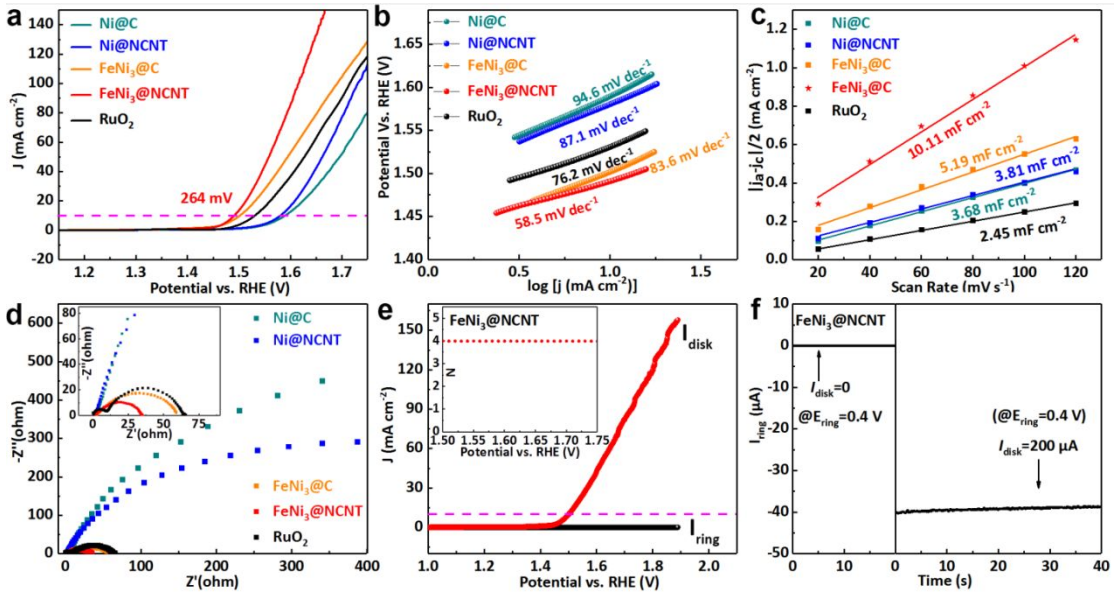


**Figure 6.** (a) Polarization curves at 5 mV $s^{-1}$, (b) Tafel plots, (c) $C_{dl}$ values, (d) EIS spectra of MOF-derived carbons and $RuO_2$. (e) RRDE voltammogram and the calculated N for **$FeNi_3$@NCNT**. (f) Ring current of **$FeNi_3$@NCNT**.

lower impedance of 34.4 Ω with a much smaller semi-circle than **Ni@C** (1790.1 Ω), **Ni@NCNT** (700.8 Ω), **$FeNi_3$@C** (59.2 Ω) and $RuO_2$ (63.3 Ω) (**Table S4**). Using a rotating ring-disk electrode (RRDE) in an $O_2$-saturated 1.0 M KOH, the ring current ($I_{ring}$) is negligible in the 1.5-1.9 V range compared to the disk current ($I_{disk}$), and the calculated average electron transfer number (N) reveals a desired quasi-4-electron OER process (**Figure 6e, S15**). In **Figure 6f**, a potential of 0.4 V is assigned to the ring electrode, and the collected $I_{ring}$ indicates approximately 38.9 μA while $I_{disk}$ is kept at 200 μA, which gives a high Faradaic efficiency (FE) of almost 100% (**Figure S16**).[33] Subsequently, this high FE was confirmed by the real-time rate of $O_2$ release monitored by Ocean Optics' standard oxygen sensors (**Figure S17**), suggesting that during the OER production nearly all the water oxidation current contributed by **$FeNi_3$@NCNT**. In order to assess the durability of the catalyst, we implemented a Chronopotentiometric examination for 10 hours, as shown in **Figure S18**. This shows no obvious attenuation with a compelling current retention of 92.4% for **$FeNi_3$@NCNT**. Moreover the as-prepared MOF-derived carbon nanomaterials present competitive OER behaviour in comparison with the previously reported electrocatalysts in **Table S5**. In this work, the high-efficiency electrochemical properties of **$FeNi_3$@NCNT** may arise from multiple comprehensive factors, including the unique hollow nanorod modified with nanotube structures, the large surface area, the abundant nitrogen content, and the synergistic effect between Ni and Fe species.[34]

Significantly, TEM/HR-TEM images of **$FeNi_3$@NCNT** show that the distinguishable lattice fringes for $FeNi_3$ and graphitic carbon layers can be clearly observed before OER. While an amorphous layer covers the margin and front edge of the composites, and the catalyst particle

inside remains relatively stable after OER (**Figure 7a**, **7c**). This phenomenon is validated by the selected area electron diffraction (SAED) patterns with the crystal phase of $FeNi_3$ involving the lattice planes of (111) and (200) in **Figure 7b**, **7d**, but the diffraction intensity decreases after the electrolysis. **Figure 7e** illustrates the schematic diagram of overall OER process that mainly occurs at the interface, where Ni-Fe alloys can be partially *in-situ* oxidized to form metal-oxygen/hydroxyl species.[35] However, the crystalline $FeNi_3$ phase dose not undergo distinct transformation after the long-time stability examination, but the peak intensity is weakened slightly in PXRD pattern (**Figure S19-S21**). Our work is solidly

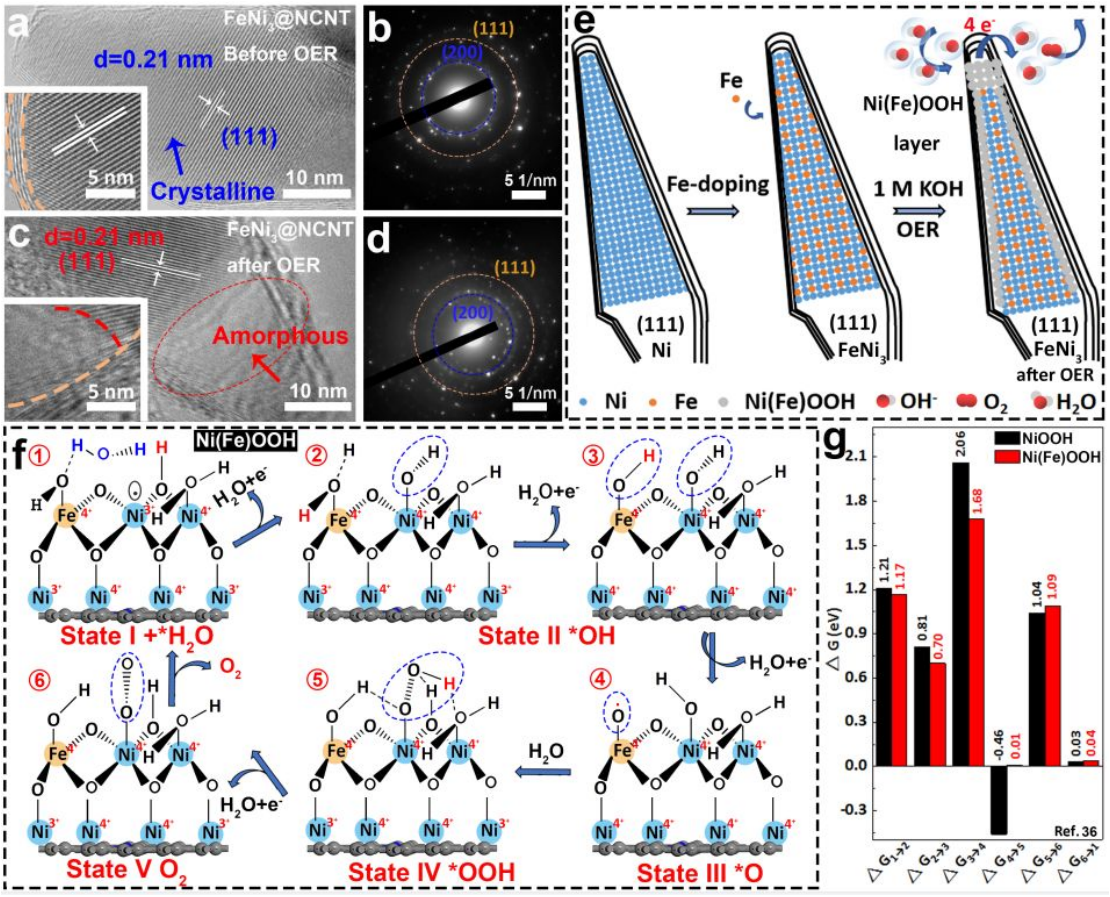


**Figure 7.** (a/c) TEM and HR-TEM images, (b/d) SAED patterns before/after OER. (e) Diagram of one $FeNi_3$ NP in one MWCNT for OER. (f) OER Mechanism on Fe-doped NiOOH. (g) The free energies for NiOOH and Ni(Fe)OOH.

and theoretically supported by a previous study, which suggests that the whole OER pathway on Fe-doped NiOOH (Ni(Fe)OOH) involves a total of six reaction steps in **Figure 7f**, all calculated Gibbs free energies are based on the Ni(Fe)OOH without considering the addition of N-doped CNTs.[36] [37] [38] We start with a $H_2O$ molecule attached to the surface of the catalyst (State I, *$H_2O$, ①), next the first oxidation-deprotonation step occurs, leading to deprotonation of the hydrogen bond on the bridge oxygen between Ni(III) and Ni(IV), and hydroxylation with the adjacent Ni(III) to form State II (*OH, ②, ~1.17 eV). Subsequently, the adsorbed $H_2O$ at the Fe(IV) site is deprotonation twice in succession to obtain intermediates of *OH (③, ~0.70 eV) and *O (State III, ④, ~1.68 eV). The high spin $3d^4$ Fe(IV) site effectively stabilizes an unpaired spin delocalized over the Fe=O bond, with unpaired spin on *O, so this facilitates the subsequent formation of an O-O bond, lowering the energy cost of this potential determining step.[39] This *O radical character enables the O-O coupling to a $H_2O$ in the first monolayer as it loses one H to an OH at an adjacent site (State IV, *OOH, ⑤). Most strikingly, the O-O coupling is facilitated by the low spin $3d^6$ Ni(IV) (0.01 eV) at an adjacent site enhancing the O-O coupling by Fe(IV) (0.46 eV). This is the origin of the synergistic effect of Ni and Fe for efficient OER that we observe experimentally. The final oxidation step involves Ni(IV), where the absorbed *OOH deprotonates to produce *$O_2$ (State V, ⑥, (1.09 eV). This $O_2$ molecule is released, allowing the surface state to revert to the initial State I through a nonelectrochemical step (0.04 eV) in **Figure 7g**. Most important, the favorable impact of Fe coupling with NiOOH regulates the defining intermediate species, that results in reducing the overpotential and enhancing the electrocatalytic OER behavior.

## 3. Conclusion

In conclusion, we report novel type of $FeNi_3$ NPs that are embedded in *in-situ* catalyzed multi-walled CNTs that are further anchored onto MOF-derived hollow N-doped carbon layers, denoted as **$FeNi_3$@NCNT**. This obtained hierarchical carbon nanomaterials are pyrolyzed from hollow **NiOF-1-Fe** precursors under the etching effect of Fe(III) on these initial **NiOF-1** nanorods with a large aspect ratio. In this case, the $FeNi_3$ alloys in **$FeNi_3$@NCNT** not only promote the efficient growth of CNTs, but they also vastly enhance the OER performance. It achieves a lower $\eta_{10}$ = 264 mV, a smaller Tafel slope of 58.5 mV $dec^{-1}$, and minimal current attenuation during the continuous 10 hour durability test compared to its control samples. Furthermore, our DFT calculation confirms that Fe coupling with NiOOH can regulate the defining intermediate species, reducing the reaction energy barrier and promoting the electrocatalytic behavior for efficient OER. This work can be easily extended to prepare the cost-effective and high-efficiency MOF-derived metal carbon nanomaterials for energy storage and conversion applications.

## Corresponding Author

*E-mail: jinjieqian@wzu.edu.cn; wag@caltech.edu

## Author Contributions

All authors contributed extensively to this work. J.Q. and W. A. G. conceived the research project. D. C. conducted the experiments and performed the characterizations. D. C., Q. S., C. H., Y. G. and Q. H. wrote the manuscript with the input from the other authors. All authors have given approval to the final version of the manuscript.

## Conflicts of interest

There are no conflicts of interest to declare.

## Acknowledgements

This work was financially supported by the Basic Science and Technology Research Project of Wenzhou, Zhejiang Province (G20190007), the Special Basic Cooperative Research Programs of Yunnan Provincial Undergraduate Universities Association (202101BA070001-042 and 202101BA070001-031). WAG acknowledges the US National Science Foundation for support (NSF CBET-2005250)

## Appendix A. Supplementary data

Supplementary material is available in the online version of this article at http://dx.doi.org/***-****-*.)

## References

[1] G. Egbert, R. Ray, Nature **2000,** *405,* 775-778.

[2] S. Chen, J. Duan, M. Jaroniec and S. Z. Qiao, *Adv. Mater.* **2014**, *26*, 2925-2930.

[3] C. Panda, P. W. Menezes, M. Zheng, S. Orthmann and M. Driess, *ACS Energy Lett.* **2019**, *4*, 747-754.

[4] G. Zhou, P. Wang, H. Li, B. Hu, Y. Sun, R. Huang, and L. Liu, *Nat. Commun.* **2021,** *12*, 4827.

[5] L. Bai, C.-S. Hsu, D. T. L. Alexander, H. M. Chen and X. Hu, *Nat. Energy* **2021**, *6*, 1054-1066.

[6] D. Chen, J. Zhu, X. Mu, R. Cheng, W. Li, S. Liu, Z. Pu, C. Lin and S. Mu, *Appl. Catal., B* **2020**, *268*.

[7] A. Grimaud, K. J. May, C. E. Carlton, Y. L. Lee, M. Risch, W. T. Hong, J. Zhou and Y. Shao-Horn, *Nat. Commun.* **2013**, *4*, 2439.

[8] G. F. Chen, T. Y. Ma, Z. Q. Liu, N. Li, Y. Z. Su, K. Davey and S. Z. Qiao, *Adv. Funct. Mater.* **2016**, *26*, 3314-3323.

[9] N. Li, L. Cai, C. Wang, Y. Lin, J. Huang, H. Sheng, H. Pan, W. Zhang, Q. Ji, H. Duan, W. Hu, W. Zhang, F. Hu, H. Tan, Z. Sun, B. Song, S. Jin, and W. Yan, *J. Am. Chem. Soc.* **2021,** 19.

[10] C. Lin, J.-L. Li, X. Li, S. Yang, W. Luo, Y. Zhang, S.-H. Kim, D.-H. Kim, S. S. Shinde, Y.-F. Li, Z.-P. Liu, Z. Jiang and J.-H. Lee, *Nat. Catal.* **2021**, *4*, 1012-1023.

[11] H. Furukawa, K. E. Cordova, M. O'Keeffe and O. M. Yaghi, *Science* **2013**, *341*, 1230444.

[12] H. F. Wang, L. Chen, H. Pang, S. Kaskel and Q. Xu, *Chem. Soc. Rev.* **2020**, *49*, 1414-1448.

[13] D. Chen, C. Han, Q. Sun, J. Ding, Q. Huang, T.-T. Li, Y. Hu, J. Qian and S. Huang, *Green Energy Environ.* **2021**, 10.1016/j.gee.2021.04.003.

[14] C. Wang, J. Kim, J. Tang, M. Kim, H. Lim, V. Malgras, J. You, Q. Xu, J. Li and Y. Yamauchi, *Chem.* **2020**, *6*, 19-40.

[15] J, Nai, B, Guan, L, Yu, X. Lou, *Sci. Adv.* **2017,** *3,* 1700732.

[16] J. Nai, J. Zhang and X. W. Lou, *Chem.* **2018**, *4*, 1967-1982.

[17] Z. Li, M. Song, W. Zhu, W. Zhuang, X. Du and L. Tian, *Coord. Chem. Rev.* **2021**, *439*.

[18] Z. Cai, Z.Wang, Y.-J. Xia, H. Lim, W. Zhou, A. Taniguchi, M. Ohtani, K. Kobiro,T. Fujita and Y. Yamauchi, *Angew.Chem. Int. Ed.* **2021,** *60,* 4747-4755.

[19] D. Ding, K. Shen, X. Chen, H. Chen, J. Chen, T. Fan, R. Wu and Y. Li, *ACS Catal.* **2018**, *8*, 7879-7888.

[20] X. Wang, L. Chai, J. Ding, L. Zhong, Y. Du, T.-T. Li, Y. Hu, J. Qian and S. Huang, *Nano Energy* **2019**, *62*, 745-753.

[21] Z. Wang, J. Ang, B. Zhang, Y. Zhang, X. Y. D. Ma, T. Yan, J. Liu, B. Che, Y. Huang and X. Lu, *Appl. Catal., B* **2019**, *254*, 26-36.

[22] J. Yan, Y. Huang, Y. Yan, X. Zhao and P. Liu, *Composites, Part A* **2020**, *139*.

[23] L. Yaqoob, T. Noor, N. Iqbal, H. Nasir, N. Zaman and K. Talha, *J. Alloys Compd.* **2021**, *850*.

[24] H. Yang, B. Wang, S. Kou, G. Lu and Z. Liu, Chem. Eng. J. **2021**, *425*.

[25] L. Chai, Z. Hu, X. Wang, Y. Xu, L. Zhang, T.-T. Li, Y. Hu, J. Qian and S. Huang, *Adv. Sci.* **2020,** 1903195.

[26] C. Yang, M. Zhou, C. He, Y. Gao, S. Li, X. Fan, Y. Lin, F. Cheng, P. Zhu, C. Cheng, *Nano-Micro Lett.* **2019**, *11*, 87.

[27] Z. Chen, R. Wu, Y. Liu, Y. Ha, Y. Guo, D. Sun, M. Liu and F. Fang, *Adv. Mater.* **2018**, *30*, e1802011.

[28] X. Zhang, W. Chen, W. Shi and P. Cheng, *J. Mater. Chem. A* **2016**, *4*, 16198-16204.

[29] J. Qian, F. Jiang, D. Yuan, M. Wu, S. Zhang, L. Zhang and M. Hong, *Chem. Commun.* **2012**, *48*, 9696-9698.

[30] Y. Xu, K. Ren and R. Xu, *Chin. J. Catal.* **2021**, *42*, 1370-1378.

[31] K. Chen, S. Kim, R. Rajendiran, K. Prabakar, G. Li, Z. Shi ,C. Jeong, J. Kang, O. Li, *J. Colloid Interface Sci.* **2021,** *582*, 977-990.

[32] S. Zou, M. S. Burke, M. G. Kast, J. Fan, N. Danilovic and S. W. Boettcher, *Chem. Mater.* **2015**, *27*, 8011-8020.

[33] T. Y. Ma, S. Dai, M. Jaroniec and S. Z. Qiao, *J. Am. Chem. Soc.* **2014**, *136*, 13925-13931.

[34] H. Xiao; H. Shin, W. A. Goddard III. Proc. Natl. Acad. Sci. U.S.A. **2018**, *115*, 5872-5877.

[35] N. Clament Sagaya Selvam, S. J. Kwak, G. H. Choi, M. J. Oh, H. Kim, W.-S. Yoon, W. B. Lee and P. J. Yoo, *ACS Energy Lett.* **2021**, *6*, 4345-4354.

[36] H. Shin, H. Xiao and W. A. Goddard, III, *J. Am. Chem. Soc.* **2018**, *140*, 6745-6748.

[37] J. Kang, X. Qiu, Q. Hu, J. Zhong, X. Gao, R. Huang, C. Wan, L.-M. Liu, X. Duan and L. Guo, *Nat. Catal.* **2021**, *4*, 1050-1058.

[38] F. L. Li, P. Wang, X. Huang, D. J. Young, H. F. Wang, P. Braunstein and J. P. Lang, *Angew. Chem. Int. Ed. Engl.* **2019**, *58*, 7051-7056.

[39] C. Kuai, C. Xi, A. Hu, Y. Zhang, Z. Xu, D. Nordlund, C.-J. Sun, C. Cadigan, R. Richards, L. Li, C.-K. Dong, X.-W. Du, and F. Lin, *J. Am. Chem. Soc.* **2021,** *143,* 18519-18526.